eprints@whiterose.ac.uk
https://eprints.whiterose.ac.uk/

Pulsations and eclipse-time analysis of HW Vir

A. S. Baran,[1]★ R. H. Østensen,[2] J. H. Telting,[3] J. Vos,[4,5] D. Kilkenny,[6] M. Vučković,[4] M. D. Reed,[2] R. Silvotti,[7] C. S. Jeffery [8] S. G. Parsons [9] V. S. Dhillon[9,10] and T. R. Marsh[11]

[1]*Uniwersytet Pedagogiczny, Obserwatorium na Suhorze, ul. Podchorążych 2, 30-084 Kraków, Polska*
[2]*Department of Physics, Astronomy, and Materials Science, Missouri State University, Springfield, MO 65897, USA*
[3]*Nordic Optical Telescope, Rambla José Ana Fernández Pérez 7, 38711 Breña Baja, Spain*
[4]*Instituto de Física y Astronomía, Universidad de Valparaiso, Gran Bretaña 1111, Playa Ancha, Valparaíso 2360102, Chile*
[5]*Institut für Physik und Astronomie, Universität Potsdam, Karl-Liebknecht-Str. 24/25, D-14476, Golm, Germany*
[6]*Department of Physics and Astronomy, University of the Western Cape, Private Bag X17, Bellville 7535, South Africa*
[7]*INAF-Osservatorio Astrofisico di Torino, strada dell'Osservatorio 20, I-10025 Pino Torinese, Italy*
[8]*Armagh Observatory, College Hill, Armagh BT61 9DG, UK*
[9]*Department of Physics and Astronomy, University of Sheffield, Sheffield S3 7RH, UK*
[10]*Instituto de Astrofisica de Canarias, E-38205 La Laguna, Tenerife, Spain*
[11]*Department of Physics, University of Warwick, Coventry CV4 7AL, UK*

ABSTRACT

We analysed recent K2 data of the short-period eclipsing binary system HW Vir, which consists of a hot subdwarf-B type primary with an M-dwarf companion. We determined the mid-times of eclipses, calculated O–C diagrams, and an average shift of the secondary minimum. Our results show that the orbital period is stable within the errors over the course of the 70 days of observations. Interestingly, the offset from mid-orbital phase between the primary and the secondary eclipses is found to be 1.62 s. If the shift is explained solely by light-travel time, the mass of the sdB primary must be 0.26 M$_\odot$, which is too low for the star to be core-helium burning. However, we argue that this result is unlikely to be correct and that a number of effects caused by the relative sizes of the stars conspire to reduce the effective light-travel time measurement. After removing the flux variation caused by the orbit, we calculated the amplitude spectrum to search for pulsations. The spectrum clearly shows periodic signal from close to the orbital frequency up to 4600 μHz, with the majority of peaks found below 2600 μHz. The amplitudes are below 0.1 part-per-thousand, too low to be detected with ground-based photometry. Thus, the high-precision data from the *Kepler* spacecraft has revealed that the primary of the HW Vir system is a pulsating sdBV star. We argue that the pulsation spectrum of the primary in HW Vir differs from that in other sdB stars due to its relatively fast rotation that is (nearly) phase-locked with the orbit.

Key words: binaries: eclipsing – stars: oscillations – subdwarfs.

1 INTRODUCTION

HW Vir is an eclipsing binary system with an orbital period as short as 2^{h}48^m consisting of a hot subdwarf B (sdB) star and a late-M dwarf (dM). The system was discovered by Menzies & Marang (1986), and has been studied extensively ever since. The light curve shows two deep minima caused by mutual eclipses of the components, and an out-of-eclipse variation interpreted as an irradiation effect. This effect is a result of two close stars having an

order-of-magnitude difference in temperature, with the M dwarf being irradiated and its upper atmosphere substantially heated by the sdB star. Menzies & Marang (1986) determined the effective temperature of the sdB to be 26 000 K and the unheated hemisphere of the dM to be ∼ 4 500 K, and suggested masses of 0.25 and 0.12 M$_\odot$ for the sdB and dM, respectively.

Multicolour photometry obtained first by Wood, Zhang & Robinson (1993) allowed modelling of the flux variation and derivation of the global parameters of the system, including temperatures, radii, and luminosities. The possibility of detecting gravitational radiation and mass loss or mass exchange inspired systematic monitoring of the eclipses. The monitoring focussed on establishing an accurate

★ E-mail: andysbaran@gmail.com

ephemeris and investigating the stability of the orbital period. Based on the Observed-minus-Calculated (O–C) variations over ∼9 years, a period change was definitely established by Kilkenny, Marang & Menzies (1994). Later, Kilkenny, van Wyk & Marang (2003a) proposed the presence of a third body in the system, orbiting the binary system with a period of nearly 21 yrs, and estimated its mass to be in the brown-dwarf mass range.

As the continued O–C monitoring revealed strong deviations inconsistent with a single planet, additional bodies in the HW Vir system were then proposed by Lee et al. (2009). The O–C diagram showed complex variation that the authors interpreted as a superposition of a parabola and two sinusoids. The former is commonly recognised as an evolutionary shortening of an orbital period, while the latter were attributed to the light–travel–time effect, in this case caused by the combined influence of two circumbinary planets. Lee et al. (2009) estimated the orbital periods of the planets to be 9 and 16 years, respectively. Soon after, Beuermann et al. (2012) published additional O–C points, demonstrating that the new data deviate significantly from the solution proposed by Lee et al. (2009). Beuermann et al. (2012) further argued that the solution proposed by Lee et al. (2009) is dynamically unstable, and proposed a new solution which they demonstrated would be stable over more than 10 Myr. Horner et al. (2012) independently made a stability analysis of the result of Lee et al. (2009), finding the same instability, but they also disputed the viability of the solution of Beuermann et al. (2012).

Since HW Vir is a bright object ($V = 10.6$), several attempts to detect the spectroscopic features of the dM companion have been made. Wood & Saffer (1999) were the first to claim such a detection, demonstrating that after having subtracted out an appropriately scaled and shifted spectrum of the primary, they could see absorption lines of $H\alpha$ moving at a velocity $275 \pm 15\,\mathrm{km\,s^{-1}}$. Since then, preliminary spectroscopic results have been presented at several conferences (Edelmann 2008; Vučković, Bloemen & Östensen 2014), but a final analysis is still pending. Edelmann (2008) obtained high-resolution spectra and also detected weak Balmer absorption features associated with the secondary, which was found to move at a velocity of $293 \pm 18\,\mathrm{km\,s^{-1}}$. Edelmann (2008) also measured the projected rotational velocity to be $74 \pm 2\,\mathrm{km\,s^{-1}}$, demonstrating that the primary is a fast rotator spinning at close to the expected rotation for a tidally bound system. Vučković et al. (2014) observed HW Vir with XShooter on the VLT, and confirmed that significant distortion of the Balmer lines caused by the irradiated side of the secondary were present in the radial-velocity curves measured from the Balmer lines.

HW Vir is the prototype of the class of post-common envelope eclipsing sdB + dM binaries. More than a dozen similar systems have been reported, and some of them have been observed over extended periods. Many more candidates are being uncovered by systematic surveys, suggesting that these systems are not uncommon (see Heber 2016, and references therein). The light-curve and radial-velocity analysis of Hilditch, Harries & Hill (1996) revealed a system with relative radii of the components of $r_1/a = 0.205$, $r_2/a = 0.211$ and at an inclination angle of $80.6°$. While the relative radii can be determined with high precision, the absolute parameters depend on the masses. Hilditch et al. (1996) inferred the masses of the primary and the secondary to be 0.5 and $0.14\,\mathrm{M_\odot}$ respectively, which gives a separation of the components, $a = a_1 + a_2$, of $0.87\,\mathrm{R_\odot}$, and the radii of the primary $R_1 = 0.178\,\mathrm{R_\odot}$ and of the secondary $R_2 = 0.183\,\mathrm{R_\odot}$.

Here, we present a study of an extensive light curve of HW Vir from data obtained with the *Kepler* spacecraft during its K2 mission.

The extreme photometric precision of the data reveals the presence of low-level pulsations in the sdB primary. This study emphasizes the derivation of primary and secondary masses based on the light travel-time effect, or Rømer delay, as measured from the offset of the secondary eclipse with respect to that of the primary, as prescribed by Kaplan (2010). This offset has hitherto only been measured with a reasonable precision in the case of the HW Vir-type system observed during the main *Kepler* mission, 2M 1938 + 4603 (Østensen et al. 2010; Barlow et al. 2012; Baran et al. 2015). A few attempts at such a determination have also been made from the ground, but never with the required precision. In this context, we also demonstrate that while *Kepler* can reach the required precision through the average of numerous subsequent eclipse timings, it is also possible to reach the required precision from the ground when sufficient signal is achieved and special care is taken when planning the observations.

While the eclipse timings provide startling indications that would contradict HW Vir being an EHB star (an extreme horizontal branch star; i.e. a star with the mass required for degenerate core-helium ignition, which corresponds to about $0.47\,\mathrm{M_\odot}$ for a solar-metalicity progenitor), the high-quality light curve also reveals a surprisingly rich pulsation spectrum. In this paper, we apply the same methods for pulsation analysis that have been successfully applied to a large number of sdB stars observed with *Kepler* (Reed et al. 2011b; Baran et al. 2012; Østensen et al. 2012; Reed et al. 2016; Kern et al. 2017). However, the pulsation analysis is inconclusive, revealing no clear spacings or splittings that can be used to identify modes.

After the pulsation analysis, we supplement this paper with hitherto unpublished ground-based data collected over recent years. We also calculate evolutionary models for post-RGB stars to determine which configurations could lead to stars at the observed location of HW Vir in the Kiel diagram. Finally, we retrieve the Gaia parallax for HW Vir and use that to discuss further constraints on the mass of the sdB primary.

2 KEPLER OBSERVATIONS

HW Vir was observed by the *Kepler* spacecraft during its *K2* mission. The observations were taken in Campaign 10, which started on 6 July 2016 and finished on 20 Sep 2016. We downloaded all available data from the "Barbara A. Mikulski Archive for Space Telescopes" (MAST).[1] The *Kepler* photometer offers two types of cadences, which are short-cadence (∼1 min), and long-cadence (∼30 min). We used short-cadence data only since they allow us to sample the orbital flux variation with a reasonable precision, and to search for pulsations in the amplitude spectrum also in the short-period region where sdB stars are known to pulsate.

During *K2*, the spacecraft is rolling as a consequence of operating with only two reaction wheels. To compensate for this roll, thrusters are fired every 5.9 h. The thruster firings and pixel-to-pixel sensitivity variation cause slow drops and spikes in the light curve. The flux variations caused by spacecraft motion are not significant when the orbital flux variation is considered but are larger than those from pulsations. First, we used standard IRAF scripts to extract fluxes from the pixel tables. Next, to remove those artifacts, we used our custom Python scripts to de-correlate fluxes measured in a target mask. This latter step removed any flux dependence on position on the CCD, and the resultant light curve was clean of thruster firing artifacts. However, prior to de-correlation, we temporarily removed

---

[1]archive.stsci.edu
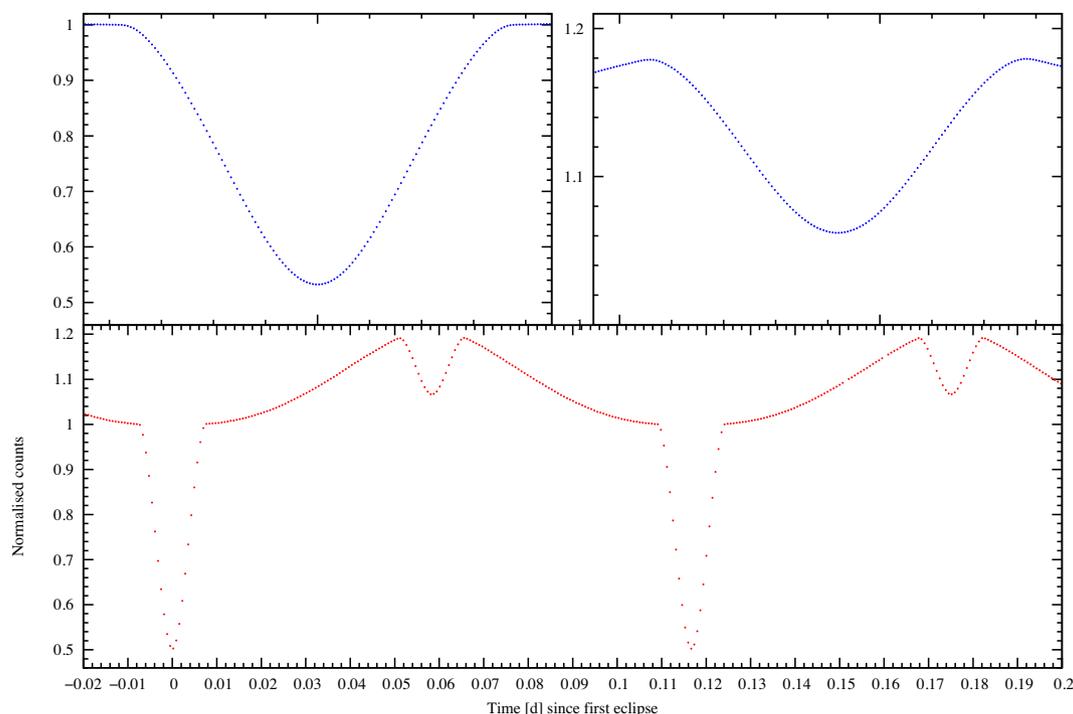
Figure 1. The first orbits of the detrended *Kepler* light curve of HW Vir (bottom). The upper panels show the primary and secondary eclipses after folding all 80 492 data points into 1 000 bins covering the orbital period. Errors are imperceptible at this precision. So are pulsations, which become evident only after removing the orbital signal.

any periodic signal that we considered intrinsic to the star, which we then added back after de-correlation. That way the de-correlation step was not affected by significant potential real variation that exists in the data. Then, we removed the first six days of data as the instrument was thermally settling during this period, and clipped the data at 4σ to remove a few outlying points. We show the final phase-folded and binned light curve in Fig. 1, together with the first cycles from the raw light curve.

3 SEARCH FOR PULSATIONS

In order to search for pulsations in the primary component of HW Vir, we first removed the orbital flux variation. To do this, we computed the amplitude spectrum and prewhitened out all frequences associated with the orbit, i.e. the orbital component and all detected harmonics thereof. This ensured that all significant contribution from mutual irradiation and eclipses was removed, but we note that any pulsation signal on the orbital frequency comb will have been lost as well. Another approach to remove the binary trend would be to model the light curve and subtract it. This approach, however, does not allow for perfect fitting of the trend, which causes the following issues. The fit of the model is not precise enough, therefore the residual data still contains periodic signal from binary trend complicating an identification of intrinsic frequencies in an amplitude spectrum, while the parameters of the binary system derived from modelling are not reliably determined.

Next, we calculated the amplitude spectrum of the orbit-subtracted residual light curve, as shown in Fig. 2. The amplitude spectrum clearly shows that HW Vir is a rich pulsator with the amplitudes of the modes being less than 0.1 ppt, far too low to be detectable in ground-based photometry. We found 91 significant frequencies stable enough to be prewhitened, and they are all listed
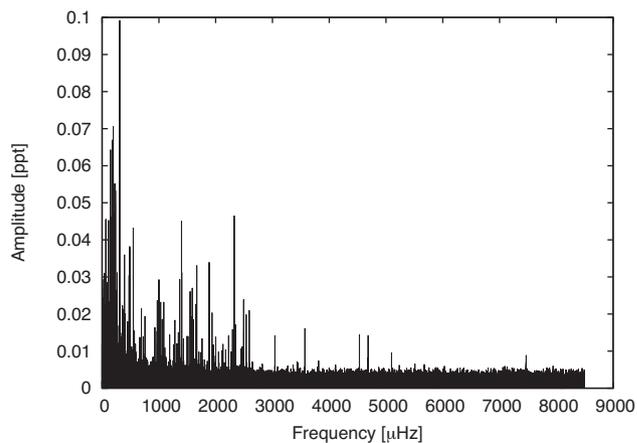
Figure 2. Amplitude spectrum of HW Vir after prewhitening of the orbital frequency comb, calculated up to the Nyquist frequency. A close-up of the region with frequencies up to 4800 µHz is shown in Fig. 3.

in Table 1. The average noise calculated from residuals level was found to be 0.0018 ppt, and we use five times this level as our detection limit.

The primary in HW Vir resembles that in 2M 1938 + 4603 presented by Østensen et al. (2010). After removal of the binary trend, the authors uncovered a rich pulsation spectrum up to the Nyquist frequency. Unfortunately, neither Østensen et al. (2010) nor Baran et al. (2015) were able to identify any of the features normally found in pulsating sdB stars and used for mode identification. This is not unexpected, since 2M 1938 + 4603 is known to be a fast rotator, and fast rotation is known to significantly shift the frequencies of rotational multiplets from the simple symmetric case.

Table 1. Frequency list of HW Vir obtained with prewhitening.

Id	Frequency [μHz]	Period [s]	Amplitude [ppt]
f_1	66.2115(38)	15103.1(9)	0.0459(18)
f_2	112.5561(39)	8884.46(31)	0.0455(18)
f_3	146.8379(27)	6810.23(13)	0.0647(18)
f_4	152.9176(42)	6539.47(18)	0.0419(18)
f_5	160.2821(39)	6239.00(15)	0.0453(18)
f_6	166.687(7)	5999.27(25)	0.0252(18)
f_7	176.8539(45)	5654.39(15)	0.0413(19)
f_8	177.0405(32)	5648.42(10)	0.0594(19)
f_9	195.6382(25)	5111.48(7)	0.0699(18)
f_{10}	203.0653(37)	4924.52(9)	0.0475(18)
f_{11}	209.463(6)	4774.10(13)	0.0303(18)
f_{12}	214.801(7)	4655.47(15)	0.0250(18)
f_{13}	217.938(9)	4588.46(19)	0.0200(18)
f_{14}	224.3393(32)	4457.53(6)	0.0553(18)
f_{15}	229.622(6)	4354.99(11)	0.0309(18)
f_{16}	259.942(7)	3847.01(10)	0.0269(18)
f_{17}	264.801(6)	3776.42(8)	0.0319(18)
f_{18}	309.2494(18)	3233.636(18)	0.1001(18)
f_{19}	349.776(11)	2858.97(9)	0.0157(18)
f_{20}	357.216(8)	2799.43(6)	0.0220(18)
f_{21}	364.425(8)	2744.05(6)	0.0218(18)
f_{22}	369.170(12)	2708.78(9)	0.0148(18)
f_{23}	376.224(12)	2657.99(8)	0.0152(18)
f_{24}	386.299(10)	2588.67(7)	0.0172(18)
f_{25}	394.0115(49)	2537.997(31)	0.0364(18)
f_{26}	407.251(9)	2455.49(5)	0.0199(18)
f_{27}	451.157(10)	2216.522(48)	0.0179(18)
f_{28}	474.504(6)	2107.463(26)	0.0303(18)
f_{29}	486.859(5)	2053.982(22)	0.0466(19)
f_{30}	486.475(7)	2055.606(30)	0.0331(19)
f_{31}	549.5331(41)	1819.727(14)	0.0433(18)
f_{32}	567.505(11)	1762.100(35)	0.0156(18)
f_{33}	663.655(13)	1506.808(29)	0.0139(18)
f_{34}	666.314(14)	1500.794(30)	0.0131(18)
f_{35}	691.356(8)	1446.432(17)	0.0216(18)
f_{36}	724.347(13)	1380.554(24)	0.0138(18)
f_{37}	755.863(9)	1322.991(16)	0.0193(18)
f_{38}	928.842(11)	1076.609(13)	0.0163(18)
f_{39}	970.037(12)	1030.888(13)	0.0144(18)
f_{40}	972.065(8)	1028.738(8)	0.0231(18)
f_{41}	1000.122(6)	999.878(6)	0.0296(18)
f_{42}	1030.472(8)	970.429(7)	0.0236(18)
f_{43}	1060.093(10)	943.314(8)	0.0187(18)
f_{44}	1085.322(8)	921.385(6)	0.0235(18)
f_{45}	1103.961(16)	905.829(13)	0.0109(18)
f_{46}	1188.621(12)	841.311(9)	0.0146(18)
f_{47}	1257.219(15)	795.406(10)	0.0118(18)
f_{48}	1280.474(10)	780.961(6)	0.0187(18)
f_{49}	1317.832(15)	758.822(8)	0.0121(18)
f_{50}	1344.634(12)	743.697(7)	0.0151(18)
f_{51}	1365.563(6)	732.2987(32)	0.0297(18)
f_{52}	1398.6840(40)	714.9578(20)	0.0448(18)
f_{53}	1401.412(6)	713.5659(30)	0.0303(18)
f_{54}	1433.665(13)	697.513(6)	0.0136(18)
f_{55}	1498.187(13)	667.473(6)	0.0141(18)
f_{56}	1512.083(13)	661.339(5)	0.0142(18)
f_{57}	1551.036(7)	644.7303(28)	0.0266(18)
f_{58}	1571.000(9)	636.5374(37)	0.0194(18)
f_{59}	1588.562(7)	629.5003(26)	0.0274(18)
f_{60}	1595.863(12)	626.6203(47)	0.0149(18)
f_{61}	1608.815(10)	621.5755(37)	0.0188(18)
f_{62}	1649.492(8)	606.2471(28)	0.0233(18)
f_{63}	1667.254(5)	599.7885(19)	0.0338(18)

Table 1 – *continued*

| Id	Frequency [μHz]	Period [s]	Amplitude [ppt]
f_{64}	1705.270(18)	586.417(6)	0.0101(18)
f_{65}	1744.336(18)	573.284(6)	0.0100(18)
f_{66}	1759.398(13)	568.3763(43)	0.0136(18)
f_{67}	1885.571(5)	530.3433(14)	0.0350(18)
f_{68}	1935.490(9)	516.6650(23)	0.0209(18)
f_{69}	1957.093(15)	510.9618(39)	0.0120(18)
f_{70}	1995.968(21)	501.010(5)	0.0088(18)
f_{71}	2001.102(13)	499.7247(32)	0.0141(18)
f_{72}	2050.786(18)	487.6179(42)	0.0103(18)
f_{73}	2115.114(17)	472.7877(38)	0.0107(18)
f_{74}	2128.599(15)	469.7927(33)	0.0121(18)
f_{75}	2177.386(17)	459.2664(35)	0.0108(18)
f_{76}	2229.054(12)	448.6208(25)	0.0146(18)
f_{77}	2272.888(18)	439.9689(34)	0.0102(18)
f_{78}	2296.967(11)	435.3568(21)	0.0163(18)
f_{79}	2326.4288(38)	429.8434(7)	0.0483(18)
f_{80}	2331.663(18)	428.8784(33)	0.0103(18)
f_{81}	2345.501(12)	426.3481(22)	0.0165(19)
f_{82}	2346.143(11)	426.2315(20)	0.0182(19)
f_{83}	2348.350(21)	425.8309(38)	0.0088(18)
f_{84}	2447.417(16)	408.5941(27)	0.0111(18)
f_{85}	2468.659(16)	405.0783(26)	0.0116(18)
f_{86}	2492.785(7)	401.1578(12)	0.0248(18)
f_{87}	2537.780(9)	394.0452(14)	0.0206(18)
f_{88}	2590.539(8)	386.0200(13)	0.0218(18)
f_{89}	3043.342(12)	328.5861(13)	0.0151(18)
f_{90}	3572.436(11)	279.9210(9)	0.0173(18)
f_{91}	4685.857(12)	213.4082(6)	0.0163(18)

In the case of HW Vir, the pulsation spectrum is rather continuous without the sparse, intermediate region around the radial fundamental that characterizes hybrid sdB pulsators with similar temperatures. Therefore, we exploited the spectrum without splitting it into g- and p-mode regions (Charpinet et al. 2000). Fig . 3 shows the regions with significant signal detected.

3.1 Multiplets

While we know from spectroscopy that the surface of HW Vir is rotating close to the orbital frequency, this does not necessarily mean that the whole star rotates with this frequency. We have seen several examples of differential rotation in pulsating sdB stars (e.g. Foster et al. 2015), so it makes sense to search for rotationally split multiplets of lower frequencies, especially among the g-modes that probe the deep interior of the stars. The high-order p-modes have high amplitudes in the outer envelope of the star (Charpinet et al. 2000), and may heretofore have a rotational splitting corresponding to the rotation period closer to the surface.

In the presence of stellar rotation, non-radial modes of degree l split into $2l + 1$ components. In case of slow rotation, i.e. when the rotational period is much longer than the pulsation period, the splitting is even and inversely proportional to the period of rotation (Charpinet et al. 2000). However, p and g modes have different constants of proportionality (the Ledoux constant), which we accounted for during our search for multiplets.

A typical rotation period for sdB stars, as derived for other pulsating sdBs observed with *Kepler*, is around 40 days. Outliers with rotation period as short as 7–10 days and as long as 90 days are known (e.g. Baran 2012; Baran et al. 2012; Telting et al. 2012;
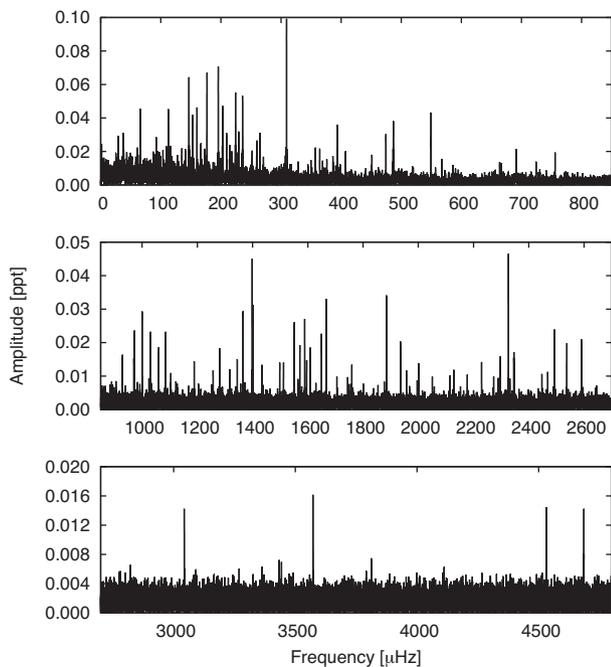
Figure 3. A close-up of the amplitude spectrum showing the region with significant signal detected.

Østensen et al. 2014; Reed et al. 2014; Foster et al. 2015). For rotation at the orbital frequency, non-linear terms become significant to the order where reliable splittings can only be determined from detailed stellar models (Aerts, Christensen-Dalsgaard & Kurtz 2010, pp. 284–290). The predicted splitting of $1/P_{rot} = 99.16\,\mu$Hz for p-modes or half of that value for dipole g-modes just gives an order-of-magnitude estimate of the expected splitting. Note that even the central component can be significantly shifted by rotation, which could potentially obscure the predicted evenly-spaced period sequence in the asymptotic limit.

We started our search for multiplets at high frequencies beyond 3000 μHz. There are only a few frequencies and the search was relatively straightforward. We plot all those frequencies in Fig. 4. We found no evidence for 99.16 μHz splitting, while the most obvious case of a possible triplet is the frequency at 4686 μHz. The off-side components are split by nearly 0.6 μHz. This splitting translates to the rotation period of ~20 days. No other frequencies show similar splitting. The one at 3043 μHz has one extra component at the higher frequency spaced by 0.4 μHz, while the frequency at 7469 μHz could be split into more than three components, being at least a quadrupole mode. The splitting of that latter frequency is not consistent with 0.6 μHz. The frequency at 3572 μHz does not show any clearly split components.

Even though some of the above examples could be multiplets, we have insufficient evidence for accepting them as rotation signatures. In 2M 1938 + 4603, Baran et al. (2015) found that most of the high-amplitude p-modes show a multiplet-like structure, and some g-modes show the same splitting as p-modes, which is inconsistent with rotational multiplets. In the case of HW Vir, the time coverage is too short to detect similar fine and super-fine fork structures. Furthermore, as clearly shown by Edelmann (2008), the Balmer line-core profiles do not support the sdB star being a slow rotator. Thus, we have no reliable evidence of rotational splittings from the high-frequency pulsations.
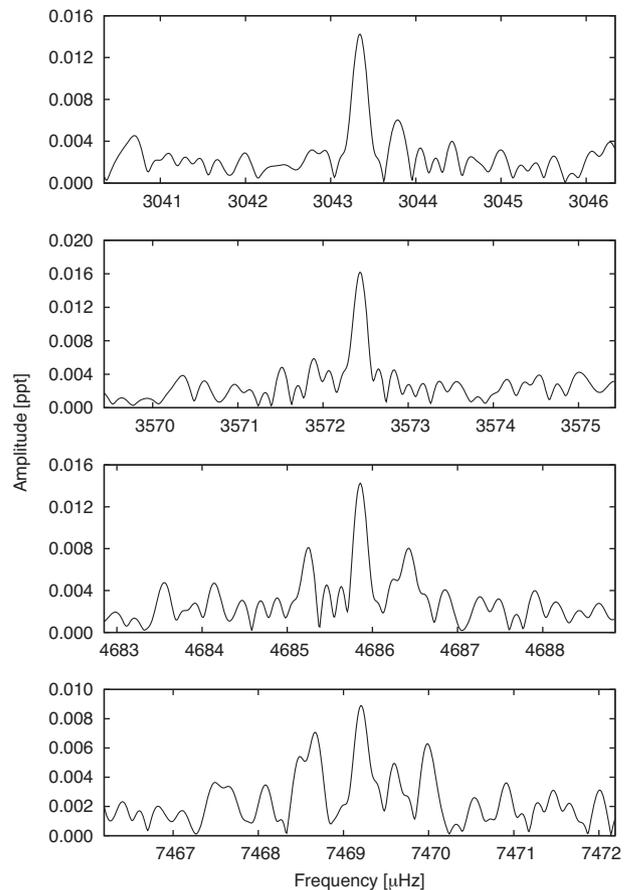

Figure 4. Close-ups of the high-frequency peaks.

We also searched for multiplets in the low-frequency region, as the rotation period of a slowly rotating core will show up in the g-modes that are probing the deepest layers of the envelope. This region is very rich in frequencies, and we checked if the splitting of 0.4–0.6 μHz, found in some p-modes, was present. We found no convincing splittings among high-amplitude peaks, but some of the lower amplitude peaks may be interpreted as showing splittings. However, they are far from convincing, and may just as well be caused by unstable amplitudes. Note that if the core rotation period was truly around 20 days, the multiplets among g-modes would remain unresolved because of their Ledoux constant. In the case of 99.16 μHz splitting, we would expect multiplet components tangled with other multiplets or single peaks. Thus, in so crowded region of frequencies, we can find random frequencies that happen to be spaced by the expected splitting by chance.

3.2 Period Spacing

The rich pulsation spectrum of the low-frequency region continues well into higher frequencies, usually associated with p-modes. It has been shown that for most pulsating sdB stars, periodograms of the region between 2 000 and 10 000 s contain sequences of evenly spaced radial overtones. These overtones are very useful for identification of modal degree since the g-mode sequences are spaced in different intervals depending on the modal degree, ℓ.

The asymptotic period spacings in sdB pulsators were predicted by Charpinet et al. (2000); however, their observational detection was only possible with the unprecedented coverage provided by
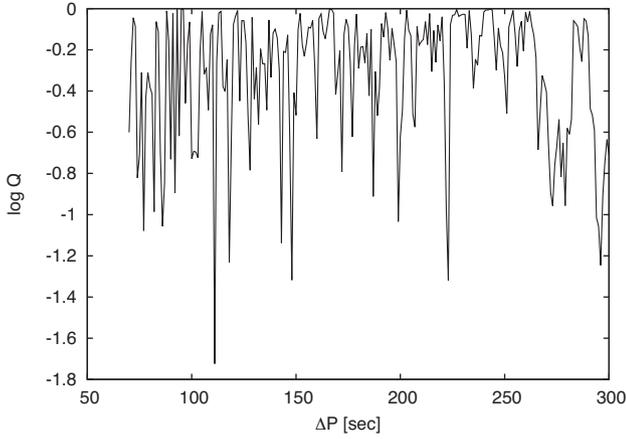
Figure 5. *Kolmogorov–Smirnov* test to find the period spacings of the same modal degree sequences. A minimum of logQ indicates a frequent spacing of 110 s.

Figure 6. The O–C diagrams for primary (top panel) and secondary (bottom panel) eclipses.

Kepler light curves. Examples of near-complete asymptotic sequences have been found in sdB pulsators as presented in Baran et al. (2012), Reed et al. (2014), Østensen et al. (2014), and Telting et al. (2014). The characteristic period spacing of dipole modes was found to be ~ 250 s, while that of quadrupole modes was found around 150 s. The $\ell = 3$ spacing is predicted to be around 110 s, but such sequences have not yet been detected.

We searched for sequences of equally spaced overtones and found some cases with the expected spacing. However, these cases do not form contiguous sequences but occur randomly throughout the spectrum, and are therefore most likely just by chance. We also calculated the Kolmogorov–Smirnov test to check for other dominant spacings in the spectrum, using the set of periods between 1800 and 8000 s. Fig. 5 shows the result of our test, and indicates that the most common spacing in period is around 110 s, but this signal is not significant. Unlike all other rich sdB pulsators observed with *Kepler*, we see no significant Q-value minimum related to the dipole or quadrupole modes. While the result of this test points towards a most common spacing as expected for modes of degree $\ell = 3$, we do not consider this evidence significant enough to make such an unexpected conclusion. It appears that the rotation rate is sufficiently high throughout the star that the rotational shifts are obscuring any sequence of evenly spaced modes. In this aspect, HW Vir resembles 2M 1938 + 4603, in which Baran et al. (2015) were unable to identify any equally spaced sequences of modes.

4 THE MID-TIMES OF ECLIPSES

To analyse the eclipses in the data, we started with the raw light curve and removed the same thruster signal that we identified in the previous section as well as all the 77 pulsation modes identified and listed in Table 1, thus obtaining a clean light curve with only the orbital signal left. We then calculated the mid-times of all the primary and secondary eclipses, using the prescription of Kwee & van Woerden (1956). We recovered 437 primary and 462 secondary eclipses. We assigned epoch numbers with each minimum and fit a line, separately, to primary and secondary minima. The derived ephemerides for the *Kepler* data are

$$T_{\text{prim}} = 2749.60746980(26)\,\text{KJD} + E \cdot 0.1167194848(7)\,\text{d} \quad (1)$$

$$T_{\text{sec}} = 2749.7825681(6)\,\text{KJD} + E \cdot 0.1167194833(16)\,\text{d} \quad (2)$$
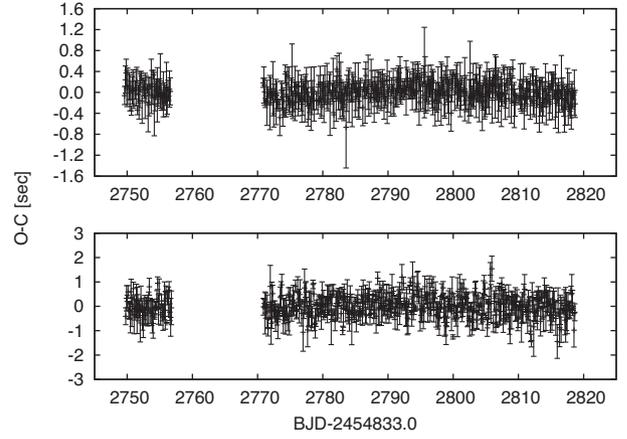
The KJDs here are Kepler mission time, which are BJD – 2454833.0.

The orbital periods for primary and secondary eclipses agree within the errors, which are 1σ fitting errors. Using these ephemerides, we calculated the O–C diagram for both primary and secondary eclipses, and we show them in Fig. 6. Since the secondary eclipses are shallower, the errors of the mid-times are larger and that is why the O–C values are spread over a larger range. Both diagrams show a flat trend and we conclude that the orbital period does not change significantly over the span of the *K2* observations.

Kaplan (2010) showed that in binary systems with components of unequal masses, the finite speed of light causes the mid-times of secondary eclipses to happen slightly more than half an orbital phase after the primary eclipses. This shift must be present unless the masses of both components are equal or the orbit has some eccentricity affecting the shift. In the case of circular orbits, the offset of the secondary eclipse is purely due to the Rømer delay. As shown by Kaplan (2010), this delay is a direct measure of the masses of both components, and the following relation applies

$$\Delta t = t_s - t_p - P/2 = \frac{P K_2}{\pi c}(1 - q) \quad (3)$$

where t_s and t_p are the measured times of secondary and primary eclipse, while q is the mass ratio, M_2/M_1, and K_2 is the orbital velocity of the secondary, which can be expressed in terms of that of the primary as $K_2 = K_1/q$, so that

$$q = \left(\frac{\pi c \Delta t}{P K_1} + 1\right)^{-1} \quad (4)$$

Thus, in the case of a circular orbit, the Rømer delay provides a direct measure of the mass ratio, when the orbital velocity of either component and the orbital period, P, is known. All these quantities can be measured, so the mass estimates are purely observational and do not require any modelling or calibrations.

We calculated the shift for 396 secondary eclipses and plotted them in Fig. 7. The average value is marked with a dashed line and corresponds to $\Delta t = 1.509(9)$ s. To obtain the mass ratio of the system, still under the assumption of a circular orbit, we adopted the radial velocity amplitude of the primary component, K_1, from Edelmann (2008) of 84.6 ± 1.1 km s^{-1}, and the orbital period from our own ephemeris. From equation (4), we obtain a mass ratio
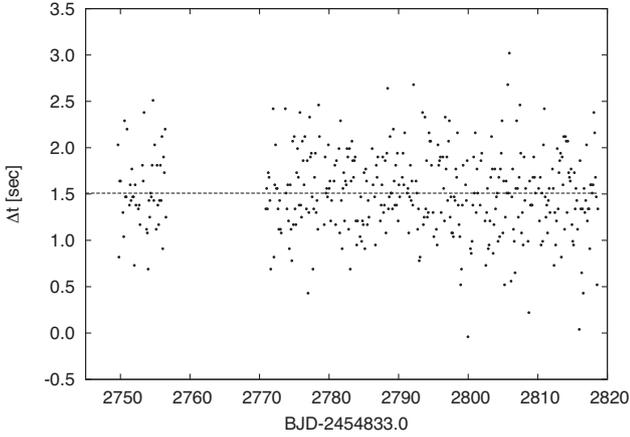
Figure 7. The shift, Δt of the secondary eclipses. The dashed line represents the average value.

$q = 0.3750$. If we propagate the errors in equation (4), we get

$$\sigma_q^2 = \frac{\pi^2 c^2 q^4}{P^2 K_1^4} \left(K_1^2 \sigma_{\Delta t}^2 + \Delta t^2 \sigma_{K_1}^2 \right), \tag{5}$$

which corresponds to $\sigma_q = 0.0034$.

Further following Kaplan (2010), we can write the relationship for the Rømer delay in terms of M_1, P, and q and solve this for M_1,

$$M_1 = \frac{\pi^2 c^3}{2 G P^2} \frac{(1+q)^2}{(1-q)^3} \Delta t^3 \tag{6}$$

we find the mass of the sdB star to be $0.262\,M_\odot$, while the mass of the M dwarf is $0.1\,M_\odot$. Propagating the errors we obtained

$$\sigma_{M_1}^2 = \left(\frac{\pi^2 c^3 \Delta t^2}{2 G P^2} \right)^2 \frac{(1+q)^2}{(1-q)^8} \left[9(1-q^2)^2 \sigma_{\Delta t}^2 + (5+q)^2 \Delta t^2 \sigma_q^2 \right] \tag{7}$$

which equals $0.007\,M_\odot$.

As mentioned, this is only strictly valid for perfectly circular orbits. Following Winn (2010) and Barlow et al. (2012), the additional delay term from eccentricity can be approximated as

$$\Delta t_e \simeq \frac{2 P e}{\pi} \cos \omega. \tag{8}$$

For the mass of the primary to be canonical ($0.47\,M_\odot$), which gives $q = 0.296$, Δt must be 2.15 s. To get an extra 0.64 s from Δt_e would require an eccentricity of only 0.0001 when ω is favourable so that its cosine is 1. We can only speculate that in such a short-period binary any large eccentricity will be damped rather quickly due to tidal dissipation, though how close to zero it will end up is unconstrained. Moreover, we do not possess any photometric or spectroscopic observations that may allow us to measure the eccentricity down to such a high precision, therefore it would be beneficial to propose a high-precision observation to pindown the eccentricity and estimate how much it contributes to the shift of the secondary eclipse.

As mentioned in Section 1, there are a few other sdB stars for which the shift of the secondary eclipse has been derived. Baran et al. (2015) reported this shift to be 1.76 s for 2M 1938 + 4603 after it had been observed for three years with the *Kepler* spacecraft, which would lead to an equally low mass of the primary. Another two stars, for which the shift was reported, were observed from the ground, but with insufficient precision to derive a reliable Rømer delay.

5 GROUND-BASED PHOTOMETRY

The eclipse–timing variability of HW Vir has been studied from the ground since the discovery of the system in 1984. In Fig. 8, we show the *Kepler* O–C points in this context. O–C variations as large as 250 s are clearly present. Our observations from SAAO (red circles; including Kilkenny et al. 1994, 2000; Kilkenny et al. 2003a), Mercator (blue boxes), Ultracam at NTT (red boxes), and the K2 points (green boxes) are indicated. Data from other sources (magenta asterisks), include data from Wood et al. (1993), Çakirli & Devlen (1999), İbanolu et al. (2004), Qian et al. (2008), Lee et al. (2009), Beuermann et al. (2012), as well as a number of points published in as IBVS notes. Note that for clarity we have omitted many points where uncertainties are reported as being high, or no errors were given, as they do not contribute significantly to the long-term trend. In order to demonstrate that the Rømer delay is readily observable with ground-based photometry, provided the required time-resolution and precision are obtained, we include some ground-based observations in this section. This also serves to improve and extend the long-term O–C data for HW Vir.
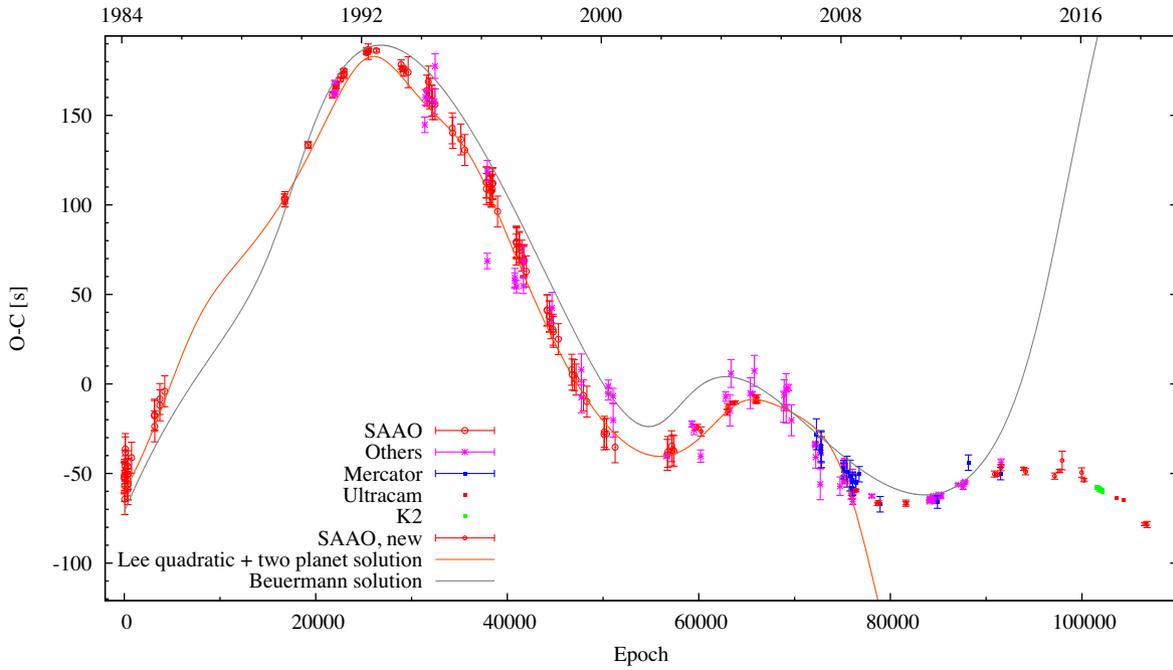
5.1 Ultracam observations

We obtained two multicolour photometry runs with Ultracam mounted on the 3.5 m NTT at La Silla. The images were processed with the provided pipeline (Dhillon et al. 2007). The first run was obtained on 17 March 2017 and covers slightly more than a full orbit. The observations started just before the mid-eclipse of the secondary and ended a bit after the completion of the consecutive secondary eclipse, as shown in the bottom panel of Fig. 9. Each point represents a single 0.497 s integration, and with a read-out delay of 0.024 s the cadence of the data is 0.521 s. The data is plotted as counts divided by those of the significantly fainter reference star (GSC 05528-00591). High-precision observations of HW Vir are a challenge as it is the brightest star in the Ultracam field-of-view on the NTT. For the first run, we had a reference star that gives only about one-sixth of the counts of the target. Still, the differential photometry with respect to this star gives a better precision than using the raw photometry, due to some light clouds, but the noise from the comparison star significantly degrades the signal. We only used g-band data, as this gave the best results. We fitted the eclipses with simple zero-centered polynomials, using only the symmetric terms

$$f(t) = a + b(t - t_e)^2 + c(t - t_e)^4 + d(t - t_e)^6 + e(t - t_e)^8. \tag{9}$$

For the secondary eclipse, we used equation (9) with $e = 0$. The measured eclipse times are given in Table 2. The RMS fitting error on the primary eclipse is only 0.094 s. However, the error of the measurement for the secondary eclipse is less good. The complete secondary eclipse at the end of the run, $t_{s,1}$, gives an error of 0.52 s, while the incomplete preceding secondary eclipse, $t_{s,0}$ gives an error of 0.89 s. When computing the Rømer delay one must have two consecutive eclipses of the same type in order to measure the instantaneous period. Since we do not have two primary eclipses, we are forced to use the secondary eclipses to estimate the period, and when propagating the errors we get the Rømer delay as

$$\Delta t = t_{s,1} - t_p - \frac{1}{2}(t_{s,1} - t_{s,0}) = 1.79 \pm 0.53s. \tag{10}$$

This measurement is perfectly consistent with the result from *Kepler*, but the error is obviously too high to make a conclusion based on ground-based data alone. However, reducing the error on the secondary eclipse timing by getting somewhat better data or getting

Figure 8. Historical O–C diagram for HW Vir, including the K2 data and new ground-based data presented here. See text for details.
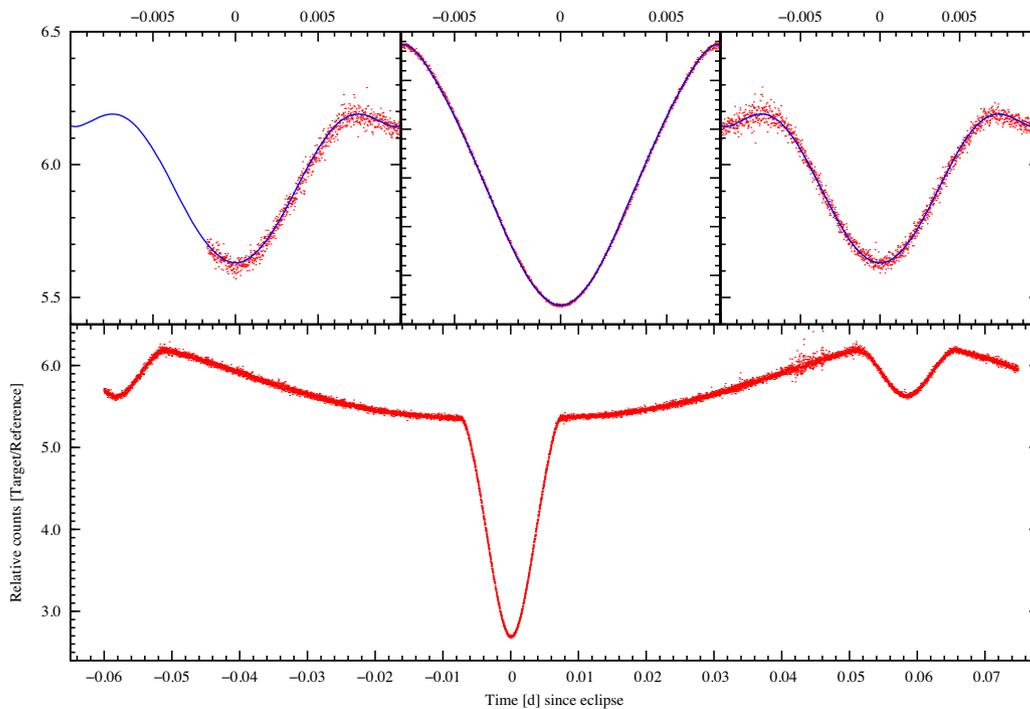
Figure 9. Ultracam light curve. The data shows observations in the *g*-band and fits to the primary and two secondary eclipses.

a few consecutive orbits would be sufficient to measure an accurate Rømer delay from the ground.

During the second observation run on June 10 2017, observations were made with a more rapid cadence of 0.1185 s (0.0945 s integration and 0.024 s readout) using no reference star, and covering primary eclipse only. After correcting the observed mid-eclipse times from UTC to BJD(TT), the resulting ephemeris point is perfectly consistent with the other recent observations, as listed in Table 2 and shown in Fig. 8. In spite of the higher

cadence, the RMS error on this observation run is slightly worse, at 0.16 s.

5.2 Mercator observations

For completeness we have also included some additional unpublished eclipse timings based on data from the 1.2-m Mercator telescope on La Palma. These observations were obtained with the Merope camera between 2007 and 2009, mostly with the RG filter,

Table 2. Times of minima from our observations.

BJD(TT)	Epoch	σ_{BJD}	Tel./Inst.
2452716.45407	59852	0.00002	SAAO-0.5m/MP
2452761.39106	60237	0.00003	SAAO-0.5m/MP
2453078.51813	62954	0.00002	SAAO-0.5m/MP
2453082.48663	62988	0.00002	SAAO-0.5m/MP
2453144.34800	63518	0.00001	SAAO-0.5m/MP
2453152.28493	63586	0.00001	SAAO-0.5m/MP
2453177.26291	63800	0.00001	SAAO-0.5m/MP
2453423.54113	65910	0.00002	SAAO-0.5m/MP
2453430.54429	65970	0.00002	SAAO-0.5m/MP
2453433.46227	65995	0.00001	SAAO-0.5m/MP
2453438.59793	66039	0.00001	SAAO-0.5m/MP
2453441.51594	66064	0.00002	SAAO-0.5m/MP
2454167.6271	72285	0.0001	Mercator/Merope
2454222.4852	72755	0.0001	Mercator/Merope
2454225.5199	72781	0.0001	Mercator/Merope
2454227.5041	72798	0.0001	Mercator/Merope
2454498.64345	75121	0.00005	Mercator/Merope
2454498.76015	75122	0.00005	Mercator/Merope
2454539.7287	75473	0.0001	Mercator/Merope
2454547.4907	75539.5	0.0002	Mercator/Merope
2454577.5458	75797	0.0001	Mercator/Merope
2454607.42597	76053	0.00005	Mercator/Merope
2454608.47643	76062	0.00005	Mercator/Merope
2454609.41015	76070	0.00005	Mercator/Merope
2454646.41028	76387	0.00005	Mercator/Merope
2454647.22802	76394	0.00001	SAAO-0.5m/MP
2454648.39450	76404	0.00005	Mercator/Merope
2454687.37888	76738	0.00005	Mercator/Merope
2454912.53141	78667	0.00001	SAAO-0.5m/MP
2454922.45258	78752	0.00001	SAAO-0.5m/MP
2454943.57804	78933	0.00005	Mercator/Merope
2454946.60914	78959	0.00005	Mercator/Merope
2455256.50385	81614	0.00001	SAAO-1m/UCTCCD
2455256.62057	81615	0.00002	SAAO-1m/UCTCCD
2455642.61128	84922	0.00004	Mercator/MeropeII
2456018.68184	88144	0.00005	Mercator/MeropeII
2456336.50979	90867	0.00002	SAAO-1m/STE3
2456372.45940	91175	0.00001	SAAO-1m/STE3
2456411.559685	91510	0.00004	Mercator/MAIA
2456415.29551	91542	0.00002	SAAO-1m/STE3
2456692.50437	93917	0.00001	SAAO-1m/STE3
2456717.48233	94131	0.00002	SAAO-1m/STE3
2457070.55886	97156	0.00002	SAAO-1m/STE3
2457130.31929	97668	0.00001	SAAO-1m/STE3
2457161.36675	97934	0.00006	SAAO-1m/STE3
2457399.59122	99975	0.00003	SAAO-1m/STE3
2457426.55338	100206	0.00001	SAAO-1m/STE3
2457829.6441621	103659.5	0.0000104	NTT/Ultracam
2457829.7025010	103660	0.0000015	NTT/Ultracam
2457829.2546024	103660.5	0.0000060	NTT/Ultracam
2457915.4913385	104395	0.0000019	NTT/Ultracam
2458165.50440	106537	0.00001	SAAO-1m/STE3
2458196.55179	106803	0.00002	SAAO-1m/STE3

with the Merope II frame-transfer camera in 2011 and 2012, also in RG, and with the 3-channel Maia camera in 2013 (Østensen 2010). The latter observations were collected in the r, g, and u bands, but due to the brightness of the target relative to the reference stars, we used the data from the r-band for the eclipse time measurement. The mid-times of the observed eclipses are all included in Table 2.

5.3 SAAO observations

Monitoring of the eclipse times of HW Vir has continued at the Sutherland site of the South African Astronomical Observatory (SAAO) since the discovery of the system, and here we include hitherto unpublished timings (Table 2). Prior to 2010 (up to epoch 78752), data were obtained with the SAAO 0.5-m telescope and Modular Photometer, which was based on a GaAs photomultiplier. All integrations were 20 s, continuous and made through a Johnson B filter. The two data points at 81614 and 81615 were from the SAAO 1-m telescope and University of Cape Town CCD camera (O'Donoghue, Koen & Kilkenny 1996) which operated in frame-transfer mode and therefore had no read-out time. All exposures were 15 s and through a B filter. The remainder of the more recent timings were made using the 1-m telescope and the SAAO STE3 camera. This has a read-out time of ∼6 s in 2x2 prebinned mode (used for all observations reported here) and with exposure times typically between 4 and 8 s, depending on atmospheric conditions, the sampling times were thus ∼10 to 14 s. Again, all data were obtained using the B filter. An outline of reduction procedures can be found in Kilkenny (2011).

5.4 The long-term evolution of the O–C

The most spectacular feature of the O–C diagram (Fig. 8) is how quickly the O–C points depart from the predicted solutions. The two-planet solution of Lee et al. (2009) is off the chart within a year of the last point included in that solution. Furthermore, the solution of Beuermann et al. (2012) diverges in the opposite direction before two observing seasons were completed. Finding a new solution that fits all of the data as well as the earlier solutions did at the time of their publication, would probably require adding another component, but should not be impossible. Still, the O–C behavior is discouraging given that after ∼34 years of observations there is still no clear periodicities present. The spectacular changes in the slope of the O–C diagram between the first 25 000 epochs, and the less dramatic oscillations during the more recent 80 000, is more reminiscent of a ringdown after a dramatic event than that of an evolutionary decay perturbed by the periodic influence of circumbinary bodies. But as for a cause of this event, we will not speculate.

6 POST-RGB EVOLUTION

In Fig. 10, we show the position of HW Vir in the Kiel diagram together with other known sdB and sdOB stars. All eclipsing sdB + dM systems with reasonably well-determined parameters are shown with error-bars. The bullets are the known pulsators from the *Kepler* mission, where the blue bullets are the V1093 Her pulsators for which the asymptotic period spacing confirms that they are EHB stars, and the green bullets are the two V361 Hya stars. All the sdB + dM binaries fall within the canonical EHB together with the sdB pulsators, except V1828 Aql, for which the primary is presumed to be a post-EHB star. The same is the case with AA Dor, which is located outside the bounds of the plot at ∼42 kK.

As we have seen in Section 4, the Rømer delay appears to favour a primary mass below 0.3 M$_\odot$, and therefore too low to sustain core-helium burning. We have therefore computed models for non-helium burning post-RGB stars along the same lines as Driebe et al. (1999), but using the stellar evolution code *Modules for Experiments in Stellar Astrophysics* (MESA v. r8845, Paxton et al. 2011,
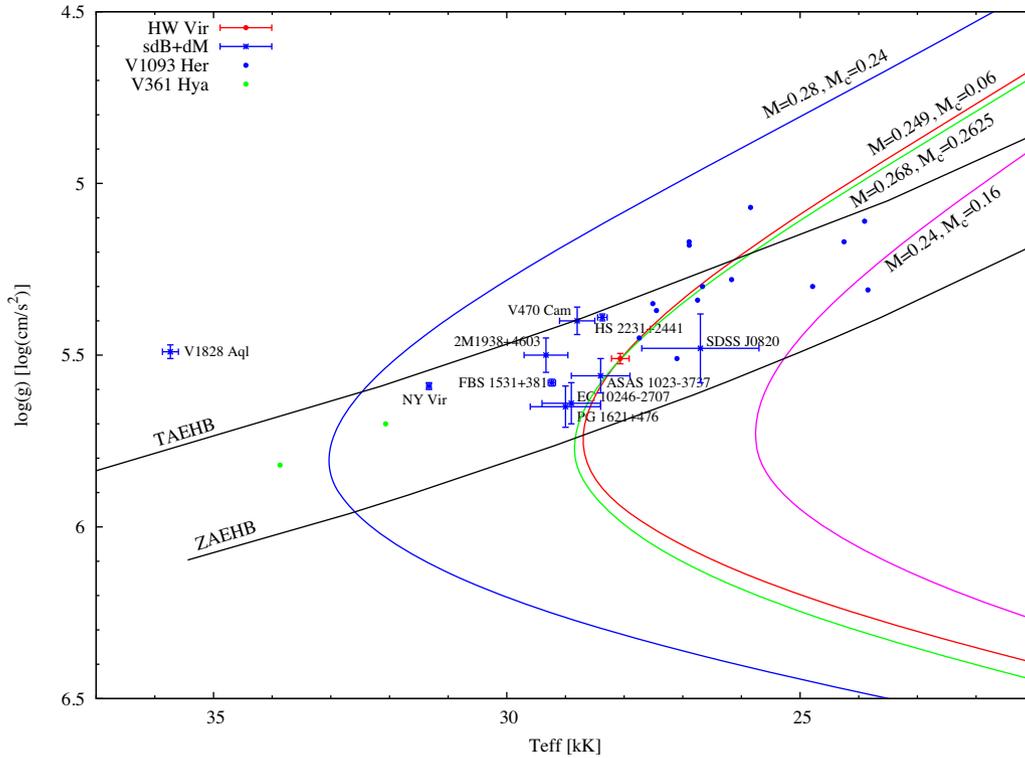
Figure 10. Kiel diagram showing the location of HW Vir (red cross; from Vučković et al. 2014) together with other known eclipsing sdB + dM systems (with error bars), as well as the pulsating EHB stars observed with *Kepler* (Blue bullets are g-mode dominated pulsators and green bullets are p-mode dominated pulsators). The post-RGB evolutionary tracks described in Section 6 pass from top to bottom of the figure. Rough boundaries indicating the ZAEHB and TAEHB are plotted, starting with a minimal envelope in the lower left and with progressively thicker envelopes on top of a 0.47 $M_\odot$ core towards the upper right. Changing metallicity or He-abundance can slightly shift the position of the EHB.

2013, 2015).[2] Even though MESA is equipped for binary evolution, common envelope (CE) evolution is not yet implemented. To simulate the evolution of post-RGB systems passing through the observed parameters of HW Vir, the CE ejection is modelled by removing the envelope of the star using a steady mass-loss rate. Thus, the calculations are split into three stages; the main-sequence evolution, the mass-loss phase, and the post-RGB evolution. The first stage ends when the core has grown to a given mass, and the second phase ends when the total mass has been reduced to a given value. During the mass-loss phase, a constant mass loss rate of $\dot{M} = 10^{-5}$ $M_\odot$/yr is enforced. In the final stage, the post-RGB star is followed from the tip of the RGB until it reaches the white dwarf cooling track at a surface gravity of $\log g = 7.0$. By varying the core mass at which mass loss starts, the envelope mass fraction at the effective temperature and surface gravity where HW Vir is located can be varied.

The post-RGB tracks reach the 'knee' at maximum temperature just below the EHB region in the Kiel diagram. Note that these post-RGB tracks spend only some ~2 Myr inside the EHB region of the Kiel diagram, while the EHB lifetime is ~100 Myr. We find that we can make tracks that pass through the location of HW Vir in the Kiel diagram for masses between 0.249 and 0.268 $M_\odot$ (see Fig. 10). The higher mass is obtained with an extremely thin envelope, while the lower mass corresponds to a thick envelope (low core mass). Thus, the mass range permitted by these post-RGB tracks is just

as narrow as the range around the canonical 0.47 $M_\odot$ mass value for EHB stars, ~±0.01 $M_\odot$. A range a few times wider could be permitted by order of magnitude deviations from solar metalicity.

While post-RGB evolution can certainly explain cases of stars found to have masses close to 0.25 $M_\odot$ that happen to overlap with EHB stars in the $T_{\rm eff}$–$\log g$ plane, it is hard to accept this solution as long as no single eclipsing sdB + dM system has been found at a higher surface gravity than the ZAEHB. Since the evolution of these stars proceeds without delay through this region, there is no reason why we should see such a large number of systems cluster in the EHB region, if their primaries are not core-helium burning stars. The mass of these stars can be determined spectroscopically if reliable lines from the secondary companions can be extracted. Then, the nature of the primary stars can be constrained more convincingly.

7 GAIA PARALLAX

HW Vir is included in Gaia DR2 (Gaia Collaboration et al. 2016, 2018; Lindegren et al. 2018) with a parallax measurement of 5.797 ± 0.085 mas, which corresponds to a distance in the range 170–175 parsec. We can infer the radius of the sdB star as

$$R^2 = d^2 \frac{F_{\rm obs}}{F_{\rm th}}, \tag{11}$$

where $F_{\rm obs}$ is the observed flux and $F_{\rm th}$ is the theoretical flux in the same bandpass. From the observed surface gravity we can then get the mass

$$M = \frac{gR^2}{G} = \frac{gd^2}{G} \frac{F_{\rm obs}}{F_{\rm th}}. \tag{12}$$

[2]The inlist for the computed MESA models can be downloaded from http://cococubed.asu.edu/mesa_market/inlists.html

Table 3. Computed masses as a function of surface gravity.

Model		Gaia *G*			SDSS *g′*	
log *g*[a]	F_{th}[b]	R [R$_\odot$]	M [M$_\odot$]	F_{th}	R [R$_\odot$]	M [M$_\odot$]
5.40	2.520	0.184	0.31	6.259	0.167	0.25
5.45	2.519	0.184	0.35	6.256	0.167	0.29
5.50	2.519	0.184	0.39	6.253	0.167	0.33
5.55	2.518	0.184	0.44	6.251	0.167	0.36
5.60	2.518	0.184	0.49	6.249	0.167	0.40
5.65	2.518	0.184	0.56	6.246	0.167	0.45

Notes. [a]Unit: log(cm s^{-2})
[b]Unit: erg cm^{-2} s^{-1} Å^{-1}/10^8

With this equation, we can infer the mass directly from the distance, whenever we have a well-calibrated observed magnitude and a surface gravity measurement and the corresponding model flux.

There are many values for the log *g* of HW Vir in the literature, and it is recognized to be quite hard to estimate the surface gravity since contamination from the secondary can fill in the Balmer lines, and rotational broadening and other effects can easily be confused with gravity broadening. Wood & Saffer ([1999](#)) report a log *g* measurement of 5.63(3) and Edelmann ([2008](#)) gives log *g* = 5.45 when taking a value close to primary eclipse. The effective temperature is more well-constrained, staying close to 28 kK. In Table [3](#) we show the masses computed from atmosphere models with different log *g*. We have done this both for the Gaia *G* magnitude, and for the SDSS *g′* magnitude from our Ultracam observations. The Gaia magnitude is orbit averaged, and the individual measurements will not be available until the final data release of Gaia (expected late 2022), so we cannot decompose the Gaia magnitude into relative contributions from the primary and secondary. But in the case of the Ultracam light curve, we can use the SDSS survey photometry (Stoughton et al. [2002](#)) of the reference star GSC 05528-00591, which has *g′* = 12.39 to calibrate the light curve of HW Vir and infer a magnitude just before and after primary eclipse of *g′* = 10.56. This is in contrast with the survey magnitude of *g′* = 10.36 from the SDSS catalogue which includes light from the irradiated secondary.

Using the zero points from Evans et al. ([2018](#)), the GAIA-G band flux is $1.451 \cdot 10^{-13}$ erg cm^{-2} s^{-1} Å^{-1}, while for the SDSS-*g′* band the observed flux is $2.970 \cdot 10^{-13}$ erg cm^{-2} s^{-1} Å^{-1}, using the zero points from Maíz Apellániz ([2007](#)). F_{th}, is obtained by integrating atmosphere models from the Tübingen NLTE Model-Atmosphere Package (Werner et al. [2003](#)).

As we see from Table [3](#), the model fluxes change very little for different log *g*, so the radius of the star is well determined from the magnitude and distance alone. However, the changes in log *g* naturally results in very large changes in mass. We can get a standard 0.47 M$_\odot$ value for the sdB if we use the Ultracam magnitude of HW Vir and a surface gravity of log *g* = 5.65. A post-RGB solution would require a surface gravity as low as 5.40.

8 DISCUSSION

8.1 Eclipse-timing delay for stars with large radii

Although the post-RGB evolutionary channel may explain the presence of HW Vir in the Kiel diagram, and the pulsation spectrum can neither confirm nor disprove the star's EHB status, the conspicuous location of HW Vir and all known similar systems on the canonical EHB makes us reluctant to jump to the immediate conclusion that HW Vir is a post-RGB star. As argued in Section 4, the Rømer delay

must be 2.15 s for the mass of the primary to be $M = 0.47$ M$_\odot$, according to the equations of Kaplan ([2010](#)). However, we may argue that those equations, while approximately valid for planets or white dwarfs in rather wide orbits, must overestimate the delay in the case of HW Vir. The following effects should all conspire to reduce the observed delay relative to the Kaplan ([2010](#)) prediction.

(1) The size of both the primary and secondary is about 20 per cent of the separation of the stars. This means that the light emitted from the substellar point on the primary is 20 per cent closer to the eclipsing disc of the secondary during primary eclipse. The same applies to the secondary eclipse. This will significantly decrease the light-travel time, and whenever the mid-point times of the eclipse is used, the relevant delay can only be estimated by applying an appropriate center-of-light distance correction to the two stars as they orbit each other. See Appendix and Fig. [11](#).

(2) With an eclipse duration of 0.122 in orbital phase, both stars move 44° along their orbit between first and last contact. Thus, at the contact points both stars are about 22° away from the axis of mid-eclipse alignment, and since this angle is not neglible, they are significantly closer to each other along the line of sight at the contact points than at mid eclipse. This effectively makes the Romer delay shorter, when mid-eclipse timings are measured from the eclipse contact points. See Fig. [12](#).

(3) The inclination of the orbit of HW Vir is known from light-curve analysis to be ∼80°, while due to the large relative sizes of the stars in the system, the substellar points are still eclipsed. The light-travel-time must therefore be reduced by a factor $1 - \sin(i)$.

(4) A beaming effect is not obvious in the orbital light-curve, as have been seen in the sdB + WD binaries (e.g. Telting et al. [2012](#)). But it must still be present at the same level, whenever the radial velocity amplitudes are comparable. The beaming effect is a harmonic function that increases the observed flux when the primary is approaching and decreases it when it is receding, so that around the time of primary eclipse it introduces an increasing slope, and at the time of secondary eclipse it is decreasing. However, around secondary eclipse the irradiated side of the companion would also be subject to beaming, and since the secondary moves much faster than the primary, the beaming is correspondingly larger. This slope would have the opposite sign and counter that of the beaming from the primary. Thus, while the beaming effect has the potential to affect the light-travel-time measurements, it cannot be estimated without proper modelling.

Ignoring beaming until all these effects can be modeled numerically, we can give an order-of-magnitude estimate of the size of the geometrical correction from points 1–3 above. The first effect is at most 20 per cent, as stated above. The second is about $1 - \cos(22°) = 7.3$ per cent. Both these effects are measured simul-
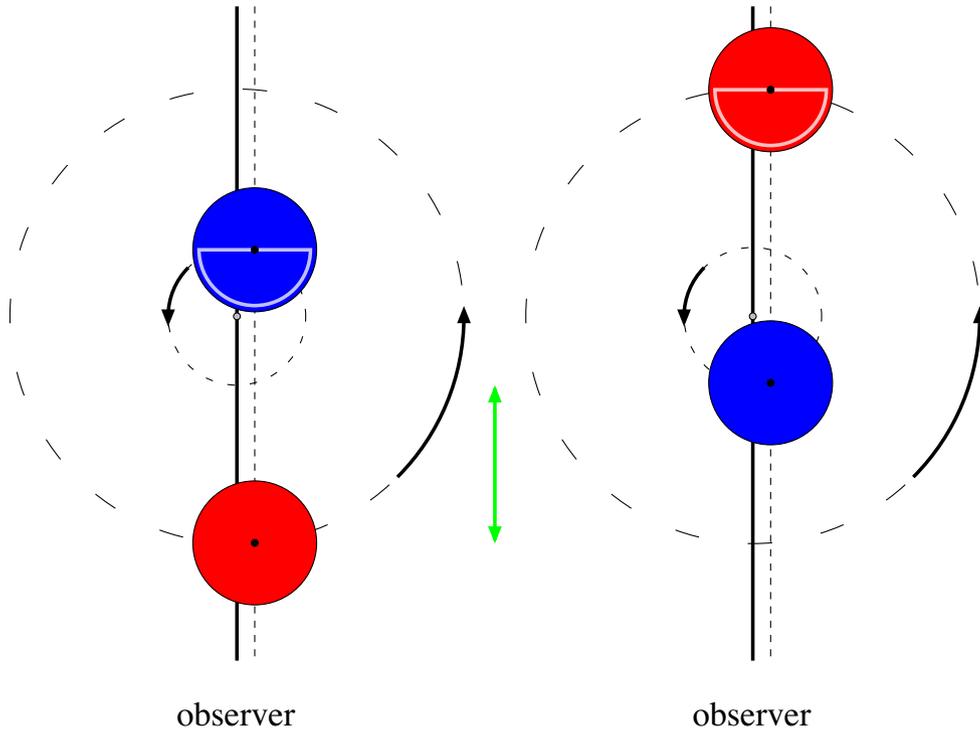
Figure 11. Sketch of the mid-eclipse geometry for HW Vir, corrected for light-travel-time effects. The hot primary is depicted in blue, the irradiated secondary in red. The thick vertical line corresponds to traditional conjunction, at orbital phases 0 and 0.5. The dashed vertical line represents the positions at which the components contribute to the eclipse. Whereas the radii and orbits are drawn to scale (radii from Hilditch et al. 1996), the offset d between the vertical lines is exaggerated for clarity. During primary eclipse (left) the primary emits its to-be-eclipsed light just before conjunction, while the secondary eclipses that light just after conjunction. Same considerations apply to the secondary eclipse (right). The difference in orbital speed of the eclipsing star, between the cases of secondary and primary eclipse, gives rise to half of the contribution to the Rømer delay discussed in Kaplan (2010): $\Delta t = t_s - t_p - P/2$. The green arrow, with size $a_2 - a_1$, measuring the offset towards the observer between the eclipsing stars at either eclipse, gives rise to the other half of the delay. This plot illustrates that for stars with large radii the to-be-eclipsed light, indicated by a half circle on the eclipsed star, originates from a closer distance to the eclipsing star than the dynamical distance between the stars. This affects the mid-eclipse geometry, and hence also the Rømer delay.

taneously when using the whole eclipse profile, so the largest of the two will be dominant. These two effects only affect the eclipse alignment, which accounts for half of the Rømer delay (Kaplan 2010; see our Fig. 11), and so combine to have a maximum effect on the Rømer delay of 10 per cent. The third effect is about $1 - \sin(80°) = 1.5$ per cent. The three together give a correction of at most 12 per cent, which would reduce the observable delay from 2.15 to 1.89 sec.

Thus, the geometrical effects from the relatively large sizes of the stars relative to their orbit can explain a significant part of the discrepancy between the observed Rømer delay and the expected value for an $0.47\,M_{\odot}$ sdB primary.

8.2 Fast rotation and the mode spectrum of sdB stars

Both HW Vir and 2M 1938 + 4603 are short-period systems, and are in fact the only two such systems with pulsating sdB/post-RGB primaries that have been observed with the *Kepler* spacecraft. The pulsation spectra of these two stars are similar; the amplitudes are low and there is no clear grouping between g- and p modes that we see in typical Kepler-observed pulsating sdB stars. Also, we do not find a g-mode period spacing in these two objects, while for the Kepler-observed sdBV stars we do. Hence, apart from the Rømer delay, also because of the remarkable pulsation amplitude spectrum the question arises if the primaries in HW Vir and 2M 1938 + 4603

are sdB stars or are of other evolutionary origin, such as post-RGB stars.

Here, we argue that the relatively fast rotation of these two stars, that have rotation periods close to the orbital period, may be the cause of the remarkable pulsation spectrum of these stars. HW Vir has a measured $v\sin i = 84.6\,\mathrm{km\,s^{-1}}$ Edelmann (2008), which implies that it is rotating at close to 12 per cent of the critical (break-up) velocity. We know from theoretical work (see e.g. Aerts et al. 2010) that rapid rotation leads to uneven multiplet splittings. In Section 3, we argue that any such splittings for HW Vir will range over large part of the Fourier spectrum, especially for high-ℓ multiplets, which makes it difficult to recognize possible multiplet frequency splittings and any possible g-mode period spacing.

Observationally we know that for some groups of pulsating main-sequence stars, with radiative envelopes as have sdB stars, that rapid rotation inhibits large amplitudes of pulsation and affects the internal mode-selection process to disfavour the lowest-degree modes; see the reviews of Breger (2000) for the case of δ Scuti pulsators, and Stankov & Handler (2005) for the case of β Cephei pulsators. Telting et al. (2006) find that from all stars with the spectral type typical for β Cephei stars, and that have $v\sin i \sim 100\,\mathrm{km\,s^{-1}}$, about 75 per cent are showing the typical Doppler-imaging signatures of modes with degrees $\ell \gtrsim 3$, as well disfavouring the lowest-degree modes. These stars have rotation rates close to 17 per cent of the critical velocity.
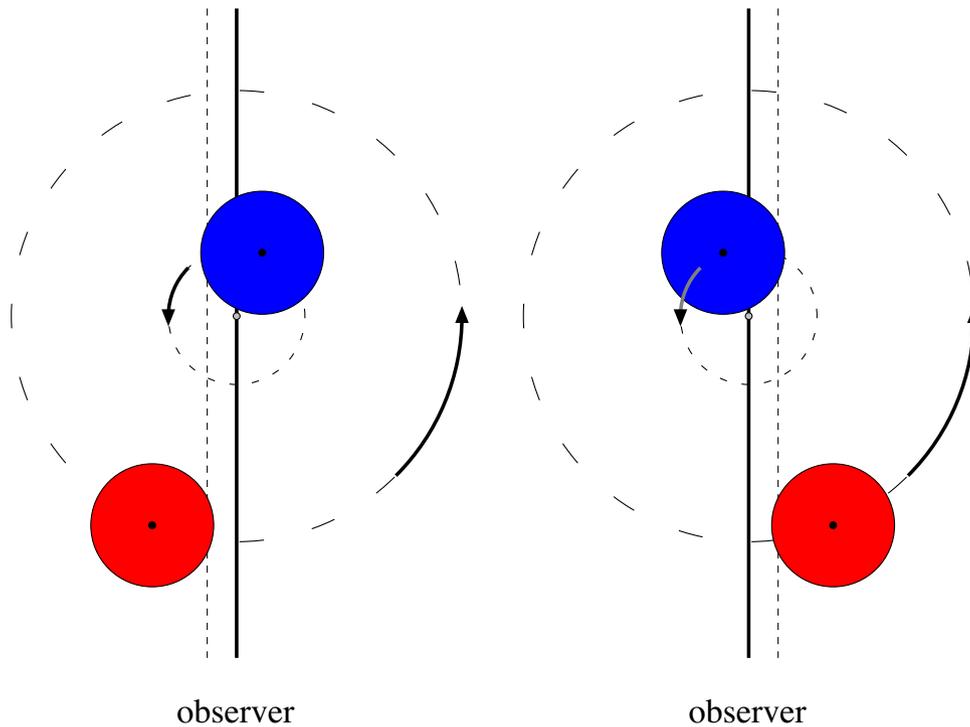
Figure 12. Eclipse ingress (left) and egress (right) geometries, with radii and orbits to scale for HW Vir. The fat vertical line corresponds to traditional conjunction. The dashed vertical lines represents the positions at the eclipse contact points. This plot illustrates that at the eclipse contact points the projected distance between the components, as seen by the observer, is smaller than the dynamical distance between the stars. This affects the Rømer delay.

We argue that it may well be that the primaries in HW Vir and 2M 1938 + 4603 are in fact genuine sdB stars, that show similar pulsation effects caused by fast rotation: low-amplitude mid-to-high-degree-ℓ modes, without clear spacings and splittings. Rotation affects the pulsations due to the Coriolis force and due to the stellar rotational oblateness. For the p-modes in HW Vir, with periods of 2–10 min, the effects of the Coriolis force may not be so large, as the rotation period is around 170 min; hence the main rotational effect that alters the pulsation-mode selection may be the departure from spherical symmetry, for those modes.

9 SUMMARY AND CONCLUSIONS

We have analysed HW Vir, an eclipsing post-common envelope binary consisting of an sdB and a dM star, observed with the *Kepler* spacecraft during the *K2* mission. The data spans nearly 70 d, interrupted by a six-day gap.

We subtracted the orbital variation and searched the light curve for pulsations. After calculating the Fourier transform, we uncovered a rich pulsation spectrum containing at least 91 significant peaks, all with amplitudes below 0.1 ppt. The spectrum shows significant peaks at both long and short periods, but longer periods are strongly favoured, with fewer peaks at high frequencies.

We searched for rotationally-induced frequency multiplets with little success. In the p-mode region, we attempted to find multiplets commensurate with the binary period. The g-mode pulsations sample deeper into the star, which required examining two separate cases; if the core is tidally locked, then we expect that high-order terms will make detecting multiplets unlikely, but we also examined the case where the core rotated subsynchronous to the binary, and commensurate with other sdBV stars. Since we did not find any of

the latter, we presume the core rotates quickly and may even be tidally locked.

We also searched for asymptotic overtones, as have been discovered in most g-mode sdBV stars. Again, we were unable to conclusively find any spacing around 250 sec that is typical of other sdBV stars. The most likely explanation is that, again, the fast rotation perturbs the frequencies, and overlapping, unevenly split multiplets complicated the search.

The pulsation spectrum of HW Vir resembles the one calculated for 2M 1938 + 4603. In neither case were multiplets or equally-spaced radial overtones detected. These two cases are very unsual. In all other Kepler-observed g-mode sdBV stars, asymptotic sequences were detected, and in most Kepler-observed sdBV stars, frequency multiplets were also detected. This can be compared with PG 1336-018 (Kilkenny et al. 2003b) and KPD 1930 + 2752 (Reed et al. 2011a), where rotationally-induced multiplets were detected in these p-mode-only pulsators.

We computed the mid-times of the eclipses and calculated an average ephemeris. The O–C diagrams show no significant variations, pointing at a stable orbital period for the duration of the *Kepler* observations. The shift of the secondary eclipses relative to those of the primary was found to be 1.51 s. Assuming a circular orbit, this shift can be interpreted as the Rømer delay, a consequence of unequal masses of the components and the finite speed of light, and – if taken at face value – a mass of the primary of $0.26\,M_\odot$ can be inferred. This mass is significantly lower than the mass required for helium core flash ignition at $\sim 0.47\,M_\odot$. While such a low value can be explained by an eccentricity of only $e \cdot \cos \omega \approx 0.0001$, the independent measurement of an equally low value in 2M 1938 + 4603 makes this interpretation less likely. If residual eccentricity were persistent in sdB + dM systems, one would expect random

orientations to produce both high and low Rømer delays with equal probability.

This is not the first time that the mass of the primary in HW Vir has been found to be low. Already, Menzies & Marang (1986), when deriving the first mass estimate for the primary, inferred a value of 0.25 $M_\odot$, and the Rømer-delay result falls surprisingly close to that value. Furthermore, the mass of the primary in 2M 1938 + 4603 was derived by Barlow et al. (2012) to be 0.37, and using the more recent Δt from Baran et al. (2015) we can infer a mass as low as 0.22 $M_\odot$, well below the required value for an EHB star and close to the value we find for HW Vir.

It is interesting that the mass we find for HW Vir is precisely 0.26 $M_\odot$, which is within the narrow band predicted by evolutionary models of post-RGB stars that have undergone the same type of common-envelope evolution as assumed for canonical sdB + dM systems, and predicted to pass through the measured position of HW Vir in the Kiel diagram. Masses that are just 0.01 $M_\odot$ higher or lower than the measured value, will not pass through this position as they contract and cool towards the white-dwarf stage. While the interpretation of HW Vir as a non-core-helium burning post-RGB star is compelling in light of the new evidence, it presents some substantial problems. The known population of sdB + dM objects is located in exactly the same part of the Kiel diagram where the canonical EHB stars reside. Post-RGB objects that fail to ignite helium in their cores should not cluster on any part of the cooling curve, although observations may be biased towards the larger and hotter objects. The fact that there are so many sdB + dM systems, and that they all mingle with the EHB population, is inconsistent with a prediction that all sdB + dM binaries should be of equally low mass to that found for HW Vir and 2M 1938 + 4603. Thus, both of the eclipsing sdB + dM systems observed with *Kepler* must either be interlopers in the EHB population, or the application of the Kaplan (2010) equations for the Rømer delay does not apply to these systems. If the former is true, and more of these systems were found to have equally low masses, one would be forced to significantly reconsider the established evolutionary scenarios in order to explain the clustering around the EHB. We find it more likely that a combination of geometrical effects not included in the Kaplan (2010) formalism conspire to make the predicted value for the light-travel-time delay too high.

We have also demonstrated that it is possible to reach the required precision to perform Rømer-delay measurements from the ground, as long as high-precision instrumentation is used, and special care is taken when planning the observations. It should therefore be possible to check the masses of many of the brighter sdB + dM systems from the ground within a reasonable time.

We have also examined the recently released Gaia data for HW Vir, but without a reliable surface gravity measurement we cannot use the parallax to measure the mass. However, the log *g* required for the parallax to yield a mass of 0.26 $M_\odot$, is ~ 5.40, lower than most measurements. The surface gravity of Wood & Saffer (1999) is consistent with a canonical mass. The most recent measurement by Vučković et al. (2014), based on VLT/Xshooter data, with a log *g* of 5.51, would yield a mass of 0.33 $M_\odot$, which is not consistent with any evolutionary scenario. Clearly, a bit more work is still required to resolve these conundrums. Fortunately, the wealth of data in the Gaia archive on hundreds of single sdB stars will allow the calibration of spectroscopic model spectra and allow us to resolve any systematic effects that may affect the surface gravity measurements.

Finally, we argue that the remarkable and similar pulsation spectra of the primaries in HW Vir and 2M 1938 + 4603, both in short-orbit binaries, differ from those in typical sdB pulsators due to the relatively fast rotation that is (nearly) phase locked with the orbit.

REFERENCES

Aerts C., Christensen-Dalsgaard J., Kurtz D. W., 2010, Asteroseismology. Springer, Berlin.
Baran A. S., 2012, AcA, 62, 179
Baran A. S. et al., 2012, MNRAS, 424, 2686
Baran A. S., Zola S., Blokesz A., Østensen R. H., Silvotti R., 2015, A&A, 577, A146
Barlow B. N., Wade R. A., Liss S. E., Østensen R. H., Van Winckel H., 2012, ApJ, 758, 58
Beuermann K. et al., 2012, A&A, 543, 41
Breger M., 2000, ASPC, 210, 3
Charpinet S., Fontaine G., Brassard P., Dorman B., 2000, ApJS, 131, 223
Çakirli Ö., Devlen A., 1999, A&AS, 136, 27
Dhillon V. S. et al., 2007, MNRAS, 378, 825
Driebe T., Blöcker T., Schönberner D., Herwig F., 1999, A&A, 350, 89
Edelmann H., 2008, in Heber U., Jeffery C. S., Napiwotzki R., eds, Astronomical Society of the Pacific Conference Series Vol. 392, Hot Subdwarf Stars and Related Objects p. 187
Evans D. W. et al., 2018, A&A, 616, 4
Foster H. M., Reed M. D., Telting J. H., Østensen R. H., Baran A. S., 2015, ApJ, 805, 94
Gaia Collaboration et al., 2018, A&A, 616, 1
Gaia Collaboration et al., 2016, A&A, 595, A1
Heber U., 2016, PASP, 128, 082001
Hilditch R. W., Harries T. J., Hill G., 1996, MNRAS, 279, 1380
Horner J., Hinse T. C., Wittenmyer R. A., Marshall J. P., Tinney C. G., 2012, MNRAS, 427, 2812
İbanolu C., Çakırlı Ö., Taş G., Evren S., 2004, A&A, 414, 1043
Kaplan D. L., 2010, ApJ, 717, L108
Kern J. W., Reed M. D., Baran A. S., Østensen R. H., Telting J. H., 2017, MNRAS, 465, 1057
Kilkenny D., 2011, MNRAS, 412, 487
Kilkenny D., Marang F., Menzies J. W., 1994, MNRAS, 267, 535
Kilkenny D., Keuris S., Marang F., Roberts G., van Wyk F., Ogloza W., 2000, The Observatory, 120, 48
Kilkenny D., van Wyk F., Marang F., 2003a, The Observatory, 123, 31
Kilkenny D. et al., 2003b, MNRAS, 345, 834

Kwee K. K., van Woerden H., 1956, Bull. Astron. Inst. Netherlands, 12, 327

Lee J. W., Kim S.-L., Kim C.-H., Koch R. H., Lee C.-U., Kim H.-I., Park J.-H., 2009, AJ, 137, 3181

Lindegren L. et al., 2018, A&A, 616, 2

Maíz Apellániz J., 2007, in Sterken C., ed., Astronomical Society of the Pacific Conference Series Vol. 364, The Future of Photometric, Spectrophotometric and Polarimetric Standardization p. 227

Menzies J. W., Marang F., 1986, in Hearnshaw J. B., Cottrell P. L., eds, IAU Symp. 118: Instrumentation and Research Programmes for Small Telescopes p. 305

O'Donoghue D., Koen C., Kilkenny D., 1996, MNRAS, 278, 1075

Østensen R. H., 2010, Astron. Nach., 331, 1026

Østensen R. H. et al., 2010, MNRAS, 408, L51

Østensen R. H. et al., 2012, ApJ, 753, L17

Østensen R. H., Telting J. H., Reed M. D., Baran A. S., Nemeth P., Kiaeerad F., 2014, A&A, 569, A15

Paxton B., Bildsten L., Dotter A., Herwig F., Lesaffre P., Timmes F., 2011, ApJS, 192, 3

Paxton B. et al., 2013, ApJS, 208, 4

Paxton B. et al., 2015, ApJS, 220, 15

Qian S.-B., Dai Z.-B., Zhu L.-Y., Liu L., He J.-J., Liao W.-P., Li L.-J., 2008, ApJ, 689, L49

Reed M. D. et al., 2011a, MNRAS, 412, 371

Reed M. D. et al., 2011b, MNRAS, 414, 2885

Reed M. D., Foster H., Telting J. H., Østensen R. H., Farris L. H., Oreiro R., Baran A. S., 2014, MNRAS, 440, 3809

Reed M. D. et al., 2016, MNRAS, 458, 1417

Stankov A., Handler G., 2005, ApJS, 158, 193

Stoughton C. et al., 2002, AJ, 123, 485

Telting J. H., Schrijvers C., Ilyin I. V., Uytterhoeven K., De Ridder J., Aerts C., Heinrichs H. F., 2006, å, 452, 945

Telting J. H. et al., 2012, A&A, 544, A1

Telting J. H. et al., 2014, A&A, 570, A129

Vučković M., Bloemen S., Östensen R., 2014, in van Grootel V., Green E., Fontaine G., Charpinet S., eds, Astronomical Society of the Pacific Conference Series Vol. 481, 6th Meeting on Hot Subdwarf Stars and Related Objects p. 259

Werner K., Deetjen J. L., Dreizler S., Nagel T., Rauch T., Schuh S. L., 2003, in Hubeny I., Mihalas D., Werner K., eds, ASP Conference Proceedings, Vol. 288, Stellar Atmosphere Modeling p. 31

Winn J. N., 2010, preprint (arXiv:1001.2010)

Wood J. H., Saffer R., 1999, MNRAS, 305, 820

Wood J. H., Zhang E.-H., Robinson E. L., 1993, MNRAS, 261, 103

APPENDIX: THE ECLIPSE-TIMING DELAY IN BINARIES WITH LARGE STARS

Kaplan (2010) discusses the Rømer delay in the case of double white dwarf binaries, for which the radii of the stars is small with respect to the orbital separation. Here, we show a simple derivation of a correction to Kaplan's Rømer delay $\Delta t = t_s - t_p - P/2$, for the case of stars with larger radii, such as the two components in HW Vir. We refer a reader to Fig. 11 to reconsider the mid-eclipse geometry. We assume an orbital inclination of 90°.

There are two conditions for having an eclipse. First, the stars need to line up towards the observer at the time that they contribute to the eclipse

$$X_1 = X_2 = d$$

with d being the distance between the eclipse alignment and conjunction (see the vertical lines in Fig. 11). Subscripts $_1$ and $_2$ refer to the primary and secondary star, while subscripts $_p$ and $_s$ refer to the primary and secondary eclipse, respectively. Secondly, the time that the to-be-eclipsed star needs to travel along distance d towards conjunction, plus the time that the eclipsing star travels along d from conjunction, equals the travel time of the light between components. At primary eclipse, the primary is eclipsed and mid-eclipse t_p occurs when the secondary reaches the eclipse alignment position d. Secondary mid-eclipse t_s occurs when the primary reaches the eclipse alignment position d.

For primary eclipse we have,

$$d/(2\pi a_1/P) + d/(2\pi a_2/P) = (a_2 + a_1)/c - \alpha_1 R_1/c,$$
$$t_p = d/(2\pi a_2/P),$$

where the rightmost term is a correction on the distance between the stars, to account for the fact that the to-be-eclipsed light is closer to the eclipsing star than the dynamical distance. For a primary star with no limb darkening $\alpha_1 = 1/3$, which limits $1/3 < \alpha_1 < 1$. Similarly, for secondary eclipse we obtain

$$d/(2\pi a_2/P) + d/(2\pi a_1/P) = (a_2 + a_1)/c - \alpha_2 R_2/c$$
$$t_s = d/(2\pi a_1/P) + P/2 + (a_2 - a_1)/c$$

where the rightmost term in the bottom equation corresponds to the green arrow in Fig. 11. For an irradiated secondary α_2 can be close to unity, implying that the observed flux is radiated from the part of the secondary that is closest to the primary.

Solving for d leads for primary eclipse to

$$d_p = 2\pi a_1 a_2/(cP) \cdot (1 - \alpha_1 R_1/(a_1 + a_2))$$
$$t_p = a_1/c \cdot (1 - \alpha_1 R_1/(a_1 + a_2))$$

and for secondary eclipse to

$$d_s = 2\pi a_1 a_2/(cP) \cdot (1 - \alpha_2 R_2/(a_1 + a_2))$$
$$t_s = a_2/c \cdot (1 - \alpha_2 R_2/(a_1 + a_2)) + P/2 + (a_2 - a_1)/c$$

Finally, for Kaplan's Rømer delay we obtain

$$\Delta t = t_s - t_p - P/2$$
$$= 2(a_2 - a_1)/c + (a_1\alpha_1 R_1 - a_2\alpha_2 R_2)/(c(a_1 + a_2))$$

where the first term on the right-hand side is the same as found by Kaplan (2010), and the second term contains corrections for the radii of the stars. In the case that both radii are equal, as is the case for HW Vir, the correction for secondary eclipse $-a_2\alpha_2 R_2/(c(a_1 + a_2))$ is dominant, and the measured delay should be shorter than predicted by Kaplan (2010).